Three-dimensional dynamic rupture simulations across interacting faults: The M w 7.0, 2010, Haiti earthquake

R. Douilly, Hideo Aochi, E. Calais, A. M. Freed

RESEARCH ARTICLE

Key Points:
- Dynamic rupture simulation of the Haiti earthquake consistent with observations
- Simulation replicates rupture propagation on fault segments
- Finite element model to simulate propagation of rupture on several faults

Correspondence to:
R. Douilly,
rdouilly@purdue.edu

Three-dimensional dynamic rupture simulations across interacting faults: The M_W 7.0, 2010, Haiti earthquake

R. Douilly[1], H. Aochi[2], E. Calais[3], and A. M. Freed[1]

[1] Department of Earth Atmospheric and Planetary Sciences, Purdue University, West Lafayette, Indiana, USA, [2] Bureau de Recherches Géologiques et Minières, Orléans, France, [3] Ecole Normale Supérieure, Department of Geosciences, UMR CNRS 8538, Paris, France

Abstract The mechanisms controlling rupture propagation between fault segments during a large earthquake are key to the hazard posed by fault systems. Rupture initiation on a smaller fault sometimes transfers to a larger fault, resulting in a significant event (e.g., 2002 *M*7.9 Denali USA and 2010 *M*7.1 Darfield New Zealand earthquakes). In other cases rupture is constrained to the initial fault and does not transfer to nearby faults, resulting in events of more moderate magnitude. This was the case of the 1989 *M*6.9 Loma Prieta and 2010 *M*7.0 Haiti earthquakes which initiated on reverse faults abutting against a major strike-slip plate boundary fault but did not propagate onto it. Here we investigate the rupture dynamics of the Haiti earthquake, seeking to understand why rupture propagated across two segments of the Léogâne fault but did not propagate to the adjacent Enriquillo Plantain Garden Fault, the major 200 km long plate boundary fault cutting through southern Haiti. We use a finite element model to simulate propagation of rupture on the Léogâne fault, varying friction and background stress to determine the parameter set that best explains the observed earthquake sequence, in particular, the ground displacement. The two slip patches inferred from finite fault inversions are explained by the successive rupture of two fault segments oriented favorably with respect to the rupture propagation, while the geometry of the Enriquillo fault did not allow shear stress to reach failure.

1. Introduction

Understanding the conditions under which an earthquake rupture may jump—or not—from one fault segment to another in complex fault systems is critical to determine why and how an initial rupture develops—or not—into a large to very large event [*Harris et al.*, 1991]. Two recent examples in transpressional fault systems illustrate rupture initiation on a small secondary thrust segment that jumped onto a longer strike-slip fault, leading to large magnitude events. A classic case is the 2002 *M*7.9 Denali earthquake, which initiated on the 48 km long Susitna Glacier blind thrust fault, jumped to the Denali strike-slip fault to rupture a 220 km long segment, and finally propagated to the Totschunda strike-slip fault for another 70 km [*Ratchkovski et al.*, 2004; *Hreinsdóttir et al.*, 2006; *Eberhart-Phillips et al.*, 2003]. Similarly, the 2010 *M*7.1 Darfield, New Zealand, earthquake initiated on the Charing Cross thrust fault, transferred to a left-lateral linking fault, and finally propagated to the main right-lateral Greendale fault [*Gledhill et al.*, 2011; *Beavan et al.*, 2012]. In contrast, there are cases where rupture initiation on a thrust fault did not propagate to a major, closely spaced, strike-slip fault. The classic example is the 1989 *M*6.9 Loma Prieta earthquake [*Dietz and Ellsworth*, 1990; *Oppenheimer*, 1990; *Beroza*, 1991; *Kilb et al.*, 1997] which ruptured a steeply dipping blind reverse fault abutting against the major strike-slip San Andreas fault but did not propagate onto that fault.

Similar to the Loma Prieta earthquake, the 2010 *M*7.0 Haiti earthquake ruptured two segments of the secondary reverse Léogâne Fault but did not transfer to the nearby Enriquillo Plantain Garden Fault (EPGF), the major plate boundary fault cutting through southern Haiti (Figure 1) [*Calais et al.*, 2010]. Had such a jump occurred, this already very destructive earthquake would have likely been an even more devastating one. Aftershock relocations delineate the Léogâne rupture on two north dipping segments with slightly different azimuths, dip angles, and overall sense of slip [*Douilly et al.*, 2013]. Finite fault inversions from teleseismic data show that rupture propagated from the eastern segment (primarily thrust) to the western segment (primarily strike slip) within only a few kilometers of the Enriquillo fault [*Mercier de Lépinay et al.*, 2011; *Meng et al.*, 2012], yet geodetic and geological observations show that no slip was triggered on that major fault. Coseismic stress changes were sufficient to induce aftershocks on the nearby offshore Trois Baies reverse fault, though again no slip was detected on that fault [*Symithe et al.*, 2013].
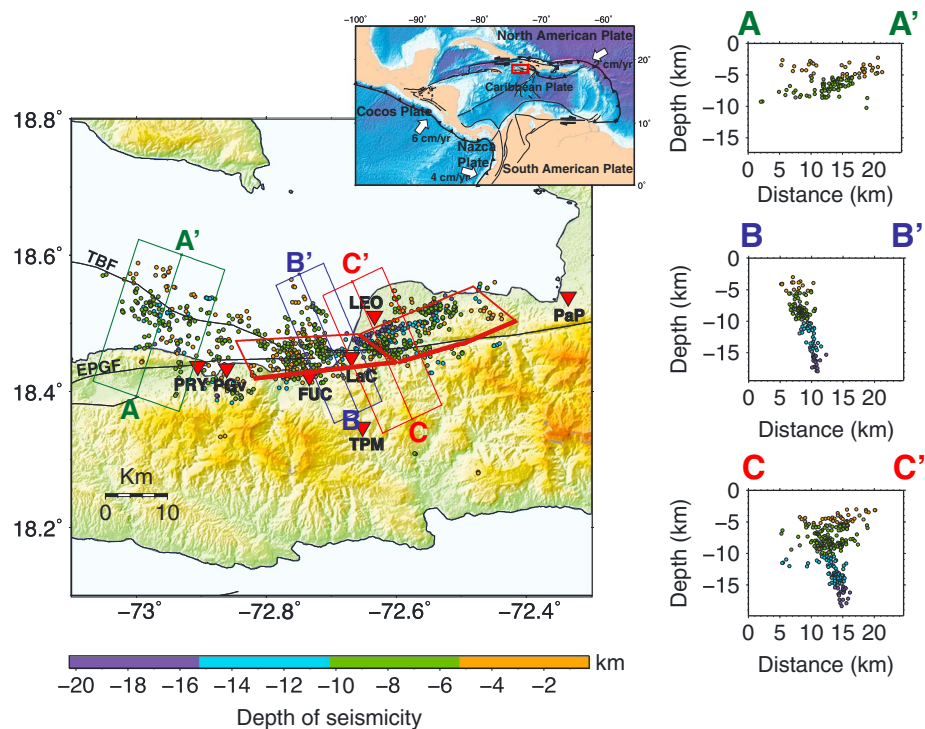
Figure 1. Aftershock distribution, cross sections, and inferred faulting model from the 2010 Haiti earthquake [after *Douilly et al.*, 2013]. The colors are coded by hypocenter depth. The black thin lines indicate the previously mapped fault trace, and the surface projection of modeled rupture segments are denoted as brown rectangle. The red triangles are the location of the chosen sites for low-frequency synthetic seismogram simulation. Aftershocks within the dashed rectangular boxes are included in the corresponding cross section. Inset: Location of the study area (red rectangle) with respect to the surrounding tectonic plates. The white arrows are the motions of the different plates with respect to the Caribbean plate.

Here we investigate the rupture process of the Haiti earthquake using dynamic simulations in order to understand why rupture propagated across the two Léogâne subsegments but not to other nearby faults, in a manner similar to the 1989 Loma Prieta earthquake. The conditions under which slip on a secondary thrust may propagate to a major plate boundary fault capable of $M > 8$ events in transpressional contexts are important to understand the seismogenic potential of such systems. We also seek to determine whether a simple rupture geometry with a single fault made of two subsegments [e.g., *Calais et al.*, 2010] is sufficient to explain the coseismic observations or whether a more complex geometry with multiple faults [e.g., *Hayes et al.*, 2010] is required. To do so we use a finite element model capable of simulating the dynamics of slip propagation based on fault geometry, fault frictional parameters, and regional stress field. Our objective is to find the set of model parameters that best explains the observed earthquake sequence in terms of geodetically and seismically inferred slip, aftershock triggering, and observed surface deformation.

2. Background

2.1. Tectonic Background: The 2010 Haiti Earthquake

The 12 January 2010 M_w7.0 Haiti earthquake struck a segment inboard of the Caribbean-North America plate boundary that had not ruptured in a significant event since a series of three events in 1701, 1751, 1770, which also caused severe damage in Port-au-Prince, Haiti's capital city [*McCann*, 2006]. Although the exact locus and magnitude of these events remains poorly constrained, they are thought to have ruptured segments of the Enriquillo Plantain Garden Fault (EPGF) running through the southern peninsula of Haiti [*Bakun et al.*, 2012]. The EPGF (Figure 1) is one of the three major faults accommodating the 19 mm/yr, east-northeastward motion of the Caribbean plate with respect to North America [*DeMets et al.*, 2000]. Global Positioning System (GPS) measurements show that this motion is partitioned in Hispaniola between plate boundary-parallel slip on the Septentrional fault and EPGF in the overriding plate, and thrust motion at the plate interface along the north Hispaniola fault zone [*Calais et al.*, 2002; *Mann et al.*, 2002]. GPS

measurements in the northeastern Caribbean and kinematic block models show that the EPGF currently accommodates 6–7 mm/yr of left-lateral strike-slip motion [*Manaker et al.*, 2008; *Calais et al.*, 2010] with a strike-normal shortening component that may be as large as 5 mm/yr [*Benford et al.*, 2012].

The source mechanism of the 2010 Haiti earthquake shows that the event generated a combination of strike slip (mostly) and reverse slip with a seismic moment of 4.4 to 4.9×10^{19} N m corresponding to M_w7.0–7.1 [*Nettles and Hjörleifsdóttir*, 2010; *Mercier de Lépinay et al.*, 2011]. Interestingly, the event did not rupture the surface but caused up to 0.6 m of regional uplift [*Hayes et al.*, 2010]. Finite fault inversions of geodetic (GPS and interferometric synthetic aperture radar (InSAR)), geological (coastal uplift), and teleseismic data show that the earthquake did not rupture the EPGF but an unmapped fault—the Léogâne fault—dipping steeply to the north and oblique to the vertical to south dipping EPGF [*Calais et al.*, 2010; *Hayes et al.*, 2010; *Mercier de Lépinay et al.*, 2011; *Meng et al.*, 2012]. Finite fault inversions show that the earthquake initiated at the eastern end of the rupture and propagated westward with two patches of high slip, an eastern one with mainly reverse dip-slip motion and a western one mainly strike slip. Overall, two thirds of the seismic moment is released by strike-slip motion and one third by dip-slip motion.

A precise relocation of aftershocks recorded by a temporary onshore/offshore seismic deployment during the 5 months following the event has been able to image the Léogâne rupture in some detail [*Douilly et al.*, 2013], showing that it consists of two segments with slightly distinct azimuth and dip angles (Figure 1). Aftershock focal mechanisms show mostly reverse fault motion on the eastern segment and strike slip on the western one, consistent with finite fault inversions. These two segments correspond to the two slip patches imaged by finite fault inversion [*Symithe et al.*, 2013]. This result is corroborated by a backprojection study [*Meng et al.*, 2012] that imaged high-frequency source radiation and found westward rupture with two subevents 35 km apart, the approximate distance between the centers of the two slip patches determined from finite fault inversions. *Meng et al.* [2012] also perform a finite fault inversion using geodetic, geological, and teleseismic data and determine a 15 s duration source time function with two subevents (corresponding to slip on the two rupture patches mentioned above), the first impulsive one, followed by a lower moment release subevent 5 s later. *Symithe et al.* [2013] show that static coseismic Coulomb stress changes increase significantly in the top part of the Enriquillo fault and to the west and east of the rupture. They also argue that the increase in Coulomb stress on the Trois Baies fault (TBF) explains the aftershocks triggered on that fault.

In the following, we use the fault geometry (Figure 1) determined in the precise aftershock relocation study of *Douilly et al.* [2013] to build and run forward models of dynamic rupture propagation and investigate the conditions under which rupture jumps, or not, to adjacent segments.

3. Model

3.1. Fault Model and Numerical Method

We aim to simulate the rupture propagation for the 2010 Haiti earthquake and understand the conditions that could lead the rupture to propagate on the Léogâne fault segments and not transfer to the other neighboring faults. We use Cubit (available from http://cubit.sandia.gov) to generate a finite element model that is 176 km long, 130 km wide, and 60 km deep, centered around the city of Léogâne (Figure 2). We approximated the fault geometry with four planar segments representing the EPGF, the East and West Léogâne faults, and the Troie Baie fault. The EPGF fault trace is well expressed in the morphology [*Mann et al.*, 1995] in the epicentral region, where *Prentice et al.* [2010] report field evidence of a 65° dip to the south, consistent with the interpretation of aftershock relocations by *Douilly et al.* [2013]. We use the strike and dip of the East and West Léogâne fault segments and Trois Baies fault derived from the spatial distribution and focal mechanism of the aftershocks of the January 2010 earthquake [*Douilly et al.*, 2013]. As we ran our forward models, we observed that the geodetic data was fit significantly better with a western Léogâne segment located 2 km to the north compared to the one in *Symithe et al.* [2013], still consistent with the scatter in aftershock hypocenters.

We discretized the model space using tetrahedral elements of 100 m size in the vicinity of the rupture that increase in size at a geometric rate of 1.03^n toward the outer regions of the mesh, where n is an integer which depends on the distance from a reference point on the eastern Léogâne segment to any point inside the medium. The final model has 4.87 millions of tetrahedral elements in total.
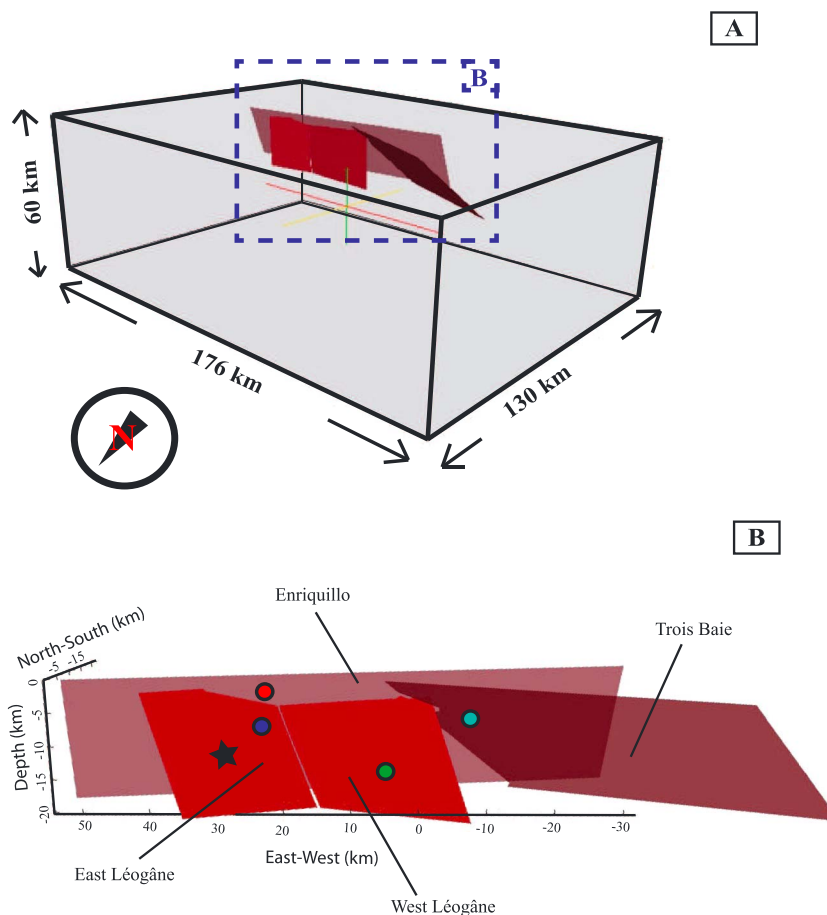
Figure 2. (a) Three-dimensional view of the fault geometry inside the domain. (b) A close-up showing the characteristics of each fault in our model. The black star is the location of the hypocenter, and the circles are locations where we evaluate shear component time histories (see Figure 15).

The fault model (Table 1) was incorporated into the Finite Element solver Pylith [*Aagaard et al.*, 2013a], which is capable of simulating quasi-static and dynamic crustal deformation, including rupture propagation. Pylith uses the conventional Finite-Element formulation for elasticity with a domain decomposition approach [*Aagaard et al.*, 2013b] similar to the "traction at split nodes" technique [*Andrews*, 1976; *Day*, 1982; *Duan and Oglesby*, 2005] and has been tested in the Southern California Earthquake Center/U.S. Geological Survey (USGS) dynamic rupture code-comparison exercise [*Harris et al.*, 2009]. For each original vertex along the negative side of a fault interface, Pylith introduces a second vertex on the positive side and a third vertex corresponding to the Lagrange multiplier needed to satisfy the constraint equation. An absorbing damper acting as a dashpot is adopted on all model boundaries except for the top (free surface) to avoid introducing artificial reflected waves. In this work we consider a semifinite homogeneous elastic medium with a 1-D elastic structure (Table 2) derived from the velocity model of *Douilly et al.* [2013]. We allow a total dynamic simulation time of 40 s with a time step interval of 0.005 s.

Table 1. Fault Geometry

Fault	Length (km)	Width (km)	Origin Point	End Point	Depth (km)	Dip
Enriquillo	86	22.4	−72.285 18.422	−73.090 18.305	20	65°S
East Léogâne	20	19.5	−72.482 18.556	−72.656 18.486	20	65°N
West Léogâne	23.4	16.9	−72.656 18.486	−72.875 18.474	20	71°N
Trois Baies	50.8	20	−72.940 18.322	−73.377 18.516	20	45°S

Table 2. Model Parameters

Model Parameters	Quantity (Units)
P and S wave velocity (α and β)	5780 (m/s); 3100 (m/s)
Density (ρ)	2700 (kg/m^3)
Radius of nucleation	2500 (m)
Slip weakening distance (D_c)	0.3 (m)
Time step	0.005 (s)

3.2. Regional Tectonic Stress

Rupture propagation on a given fault and the triggering of neighboring fault segments depend in part on the initial stress state of each fault. We have no direct estimate of principal stresses in southern Haiti but know that the tectonic regime combines strike slip and thrust faulting. We therefore consider that the maximum principal stress direction is horizontal. We used a trial-and-error approach by varying the orientation of the maximum stress direction (N90°W to N90°E) to find the optimum direction and amplitude of the stress axes consistent with the known slip direction of each fault segment, which was estimated from the focal mechanisms study of *Douilly et al.* [2013], supposing that a regional stress field is globally unchanged before and after the 2010 earthquake. Doing so, we related the principal strain components using the shape factor R [*Angelier*, 1990; *Aagaard et al.*, 2004] to the principal stress (without the isotropic lithostatic component):

$$R = \frac{\epsilon_1 - \epsilon_2}{\epsilon_1 - \epsilon_3} \quad \text{where} \quad \epsilon_1 = 6e^{-4} \quad and \quad \epsilon_2 = 1e^{-4} \tag{1a}$$

$$\begin{bmatrix} \sigma_1 \\ \sigma_2 \\ \sigma_3 \end{bmatrix} = \begin{bmatrix} \lambda + 2\mu & \lambda & \lambda \\ \lambda & \lambda + 2\mu & \lambda \\ \lambda & \lambda & \lambda + 2\mu \end{bmatrix} \begin{bmatrix} \epsilon_1 \\ \epsilon_2 \\ \epsilon_3 \end{bmatrix} \tag{1b}$$

where ϵ is the principal strain, σ is the principal stress, and λ and μ are the Lamé parameters.

In the following, we test two cases of regional tectonic stress: one where stress is independent of equations (1a) and (1b) with uniform shear and normal stress applied to all the faults (scenarios O1 and O2), the other where principal stresses obey equations (1a) and (1b) with three subcases: $R = 0.4$ (scenario A), $R = 0.6$ (scenario B), and $R = 0.8$ (scenario C).

Slip vectors are usually colinear with the direction of the applied shear stresses on each fault [*Angelier*, 1979; *Gephart and Forsyth*, 1984]. Therefore, we can estimate the direction (azimuth) of the maximum principal stress so that the loading shear traction is consistent with the slip direction observed on the Léogâne segments during the 2010 Haiti earthquake. We find that (1) the stress orientation does not change significantly among scenarios when we vary the tectonic regime (Table 3), and (2) a maximum principal stress direction of N60±10°E agrees well with the observed motion on the faults, as shown in Figures 3a–3c for scenario B. Therefore, we consider in the following two values for the principal stress orientation (N50°E and N60°E). Those directions of the maximum principal stress are consistent with the expected stress regime of a left-lateral transpressional context with generally E-W striking faults, as indicated by geodetic studies [*Calais et al.*, 2010; *Benford et al.*, 2012].

The estimated N50°E and N60°E maximum principal stress direction, however, do not satisfy observations for the Trois Baies fault (Figures 1 and 3d). We must therefore rotate the stress tensor on that fault by N30±5°E in order to match the observed reverse shear tractions. This is corroborated by an inversion of the focal mechanisms of aftershocks on the Troies Baie fault for a deviatoric stress tensor using the technique of *Hardebeck and Michael* [2006], which gives a horizontal maximum principal stress with a 30° azimuth. A similar calculation for the focal mechanisms on the eastern (respectively western) segment of the Léogâne fault indicates an horizontal maximum principal stress of 83° (respectively 75°) azimuth. Though the 75°

Table 3. Shear Stress Information for Scenarios A, B and C

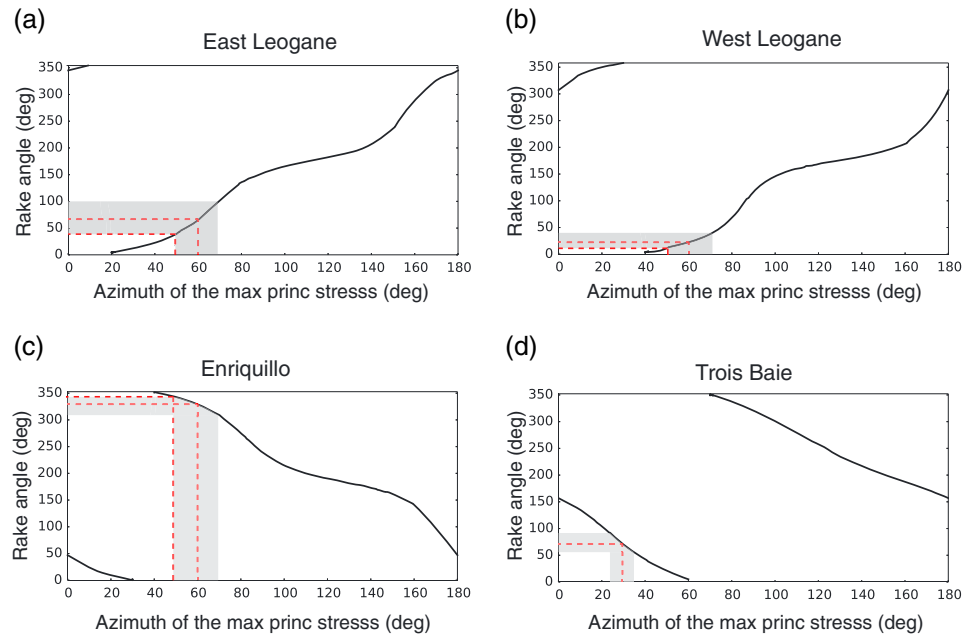|	Scenario A (R = 0.4)				Scenario B (R = 0.6)				Scenario C (R = 0.8)			
	EL	WL	EN	TB	EL	WL	EN	TB	EL	WL	EN	TB
Shear Stress Rake (deg)	56°	12°	18°	77°	66°	22°	30°	70°	48°	20°	333°	85°
Shear Stress Mag (MPa)	10.74	21.50	19.37	18.14	9.84	15.07	14.18	8.26	11.05	13.88	13.49	3.00
Sliding Stress (MPa)	1.82	5.71	5.71	5.71	1.82	2.85	2.85	2.85	1.82	3.63	3.63	3.63
Failure Stress (MPa)	18.16	57.08	57.08	57.08	18.16	28.54	28.54	28.54	18.16	33.73	33.73	33.73

Figure 3. (a–d) Azimuth of the maximum principal stress with respect to the rake angle on each fault for scenario B ($R = 0.6$). The dashed red lines indicate the azimuth (50° and 60°) deduced for our simulation, and the grey regions indicate the observation range.

azimuth is slightly greater than the 50–60° of our estimation, this might confirm the hypothesis of the possible counterclockwise rotation of the principal stress across this region. We acknowledge that the ambient stresses calculated here could be biased because aftershocks result from a stress field modified by the main shock. However, the fact that the strain rate field derived from interseismic geodetic measurements in Haiti is consistent with the 2010 earthquake coseismic source [*Calais et al.*, 2010] suggests that the bias is small. Additional work is needed to better determine the regional background stress independently from the 2010 earthquake aftershock sequence.

After estimating the principal stress, we rotated it from the principal stress coordinate system to the east-north-up coordinate system (σ_d) and superimposed the depth-dependent lithostatic overburden pressure ($\rho g h$), which prevents faults from opening. The total stress is therefore given by the following:

$$\sigma = \sigma_d + \begin{bmatrix} \rho g h & 0 & 0 \\ 0 & \rho g h & 0 \\ 0 & 0 & \rho g h \end{bmatrix} \quad (2)$$

where ρ is medium density, g is gravitational acceleration, and h is depth. The resulting stress tensor is then used to calculate the initial normal and shear tractions on each fault in the model. The initial loading tractions for each fault are summarized in Table 3.

3.3. Rupture Criterion and Friction Law
We consider a slip weakening friction law [*Ida*, 1972; *Andrews*, 1976] with Coulomb rupture criterion. The resistance of the interface is given by a product of the normal stress σ_n and a friction coefficient μ_f:

$$\mu_f = \begin{cases} \mu_{\text{dynamic}} + \left(1 - \frac{D}{D_c}\right)(\mu_{\text{static}} - \mu_{\text{dynamic}}) & \text{if } D \leq D_c \\ \mu_{\text{dynamic}} & \text{if } D > D_c \end{cases} \quad (3)$$

where D is slip, D_c is the slip weakening distance, and $\mu_{\text{dynamic}}/\mu_{\text{static}}$ are the dynamic/static friction coefficients. We consider a depth-dependent normal traction and assume that friction coefficients vary inversely with depth in order to assure a constant stress drop throughout each fault (Figure 4 [*Aagaard et al.*, 2001]), namely

$$\mu_{\text{static}} = \frac{b \rho \beta^2}{\sigma_n} \text{ and } \mu_{\text{dynamic}} = 10^{-1} \mu_{\text{static}} \quad (4)$$
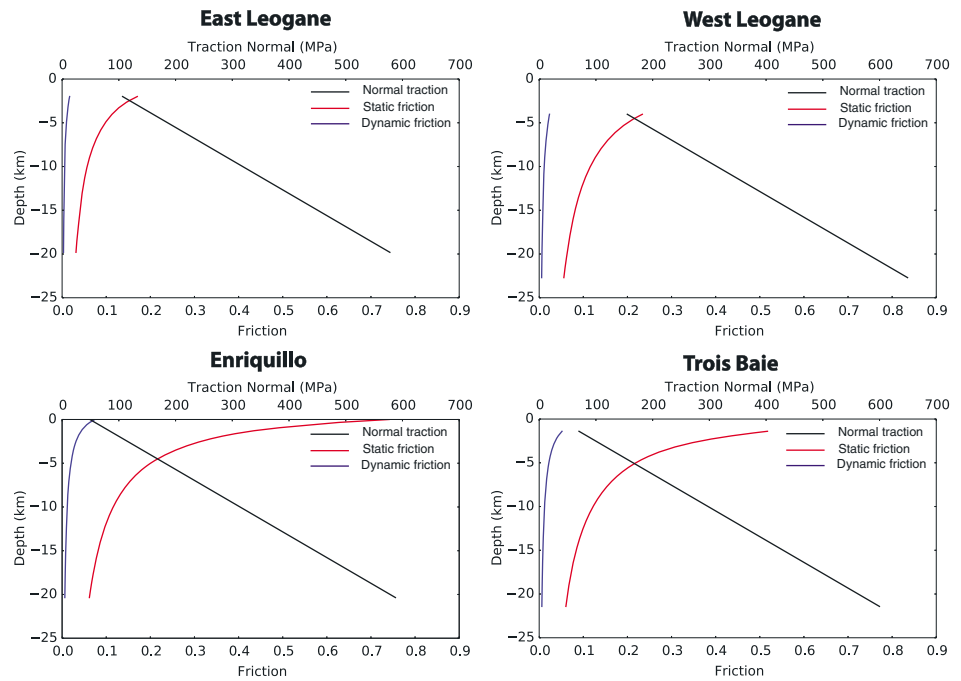
Figure 4. Normal traction (black), static (red), and dynamic (blue) coefficients of friction on each fault for scenario B.

where β is the shear velocity and b is a constant. The shear modulus is equal to $\rho\beta^2$, and the frictional resistances are defined as its fractions with a coefficient b for static friction and $0.1b$ for dynamic friction. We consider a range of values for b for each scenario type and for the two chosen values of the principal stress orientation (N60°E and N50°E).

Because of the orientation of the eastern Léogâne segment with respect to the principal stress, loading shear traction on that segment is much smaller than on the western segment or on the EPGF (Table 3). We recall that if the loaded shear stress on a fault (τ_l) is equal or less than the sliding stress ($\tau_s = \sigma_n \cdot \mu_{\text{dynamic}}$), rupture dies out rapidly without propagating spontaneously over the entire fault. On the other hand, if shear stress is closer to failure stress ($\tau_f = \sigma_n \cdot \mu_{\text{static}}$), then rupture may propagate and break the entire fault. Therefore, the loading shear stress must lie between sliding and failure stress for the rupture to propagate a significant distance [*Das and Aki*, 1977; *Aagaard et al.*, 2001]. Therefore, if all the faults had the same frictional parameters in the model, rupture initiation on the eastern Léogâne segment, as observed seismologically, would be very difficult and would not propagate to the western segment, resulting in low slip incompatible with observations. In order for the rupture to have propagated along the entire Léogâne fault, as inferred from geodetic and seismological observations, we surmise that frictional parameters must have been lower on the eastern Léogâne segment than on the other segments (Figure 4).

We introduce a uniform slip weakening distance D_c of 0.3 m, implying that fracture energy is unchanged with depth. In order to start the rupture process, we introduce a circular patch of 2.5 km radius in the middle of the eastern Léogâne segment where shear stress is 5% greater than failure stress [*Day*, 1982; *Madariaga et al.*, 1998].

The exploration on the parameter values described above generates a total of 180 simulations (Figure 5). We score each simulation using its weighted RMS (WRMS) metrics:

$$\text{WRMS} = \sqrt{\frac{1}{m}\frac{\sum_{1}^{m}\frac{(d_o - d_c)^2}{\sigma^2}}{\sum_{1}^{m}\frac{1}{\sigma^2}}} \tag{5}$$
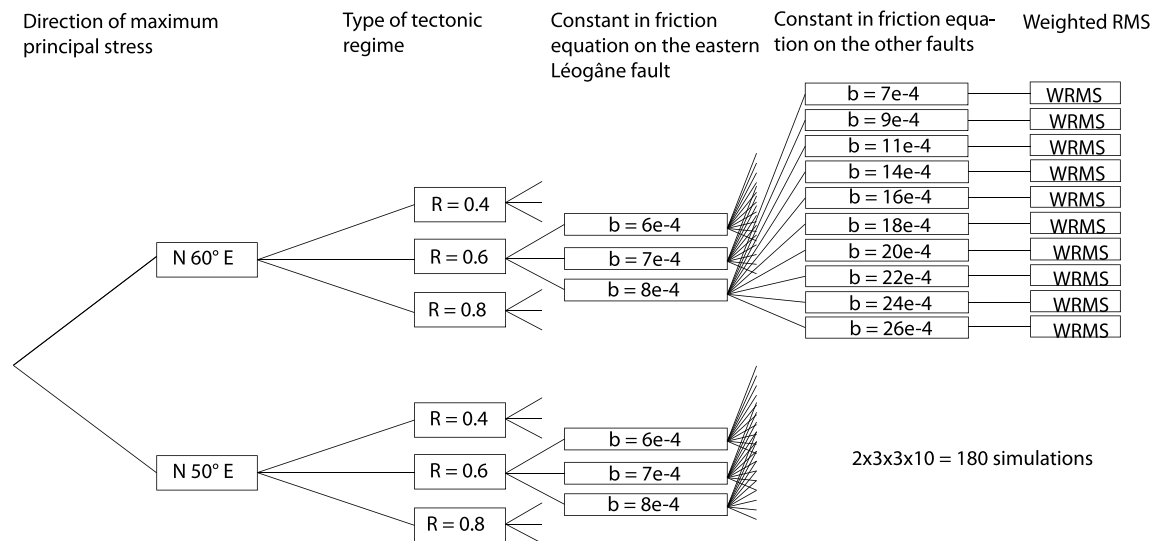
Figure 5. Schematic approach for the different dynamic rupture simulations. Each choice of parameters is explained in the text.

where d_o and d_c are the observed and calculated displacements, σ is the observational variance, and m is the total number of observations. We score the models against finite static displacements from GPS, InSAR, and coastal uplift data as no near-field coseismic seismological observation exists in the epicentral area.

Figures 6 and 7 show the WRMS misfit for the GPS and coastal uplift data sets as a function of the b friction constant on the eastern (weaker) Léogâne segment and on other fault segments. We find the lowest WRMS for a maximum principal stress azimuth of 60° for $R = 0.4$ and $R = 0.6$ and of 50° for $R = 0.8$. We therefore perform the dynamic rupture simulations described below for the case, from each scenario, that leads to the lowest WRMS misfit.

4. Simulation Results

4.1. Uniform Shear and Normal Stress on All Faults

Before proceeding to the three cases described in the previous section, we first show a simple simulation where stress and friction are constant with depth and do not account for the regional tectonic setting. We
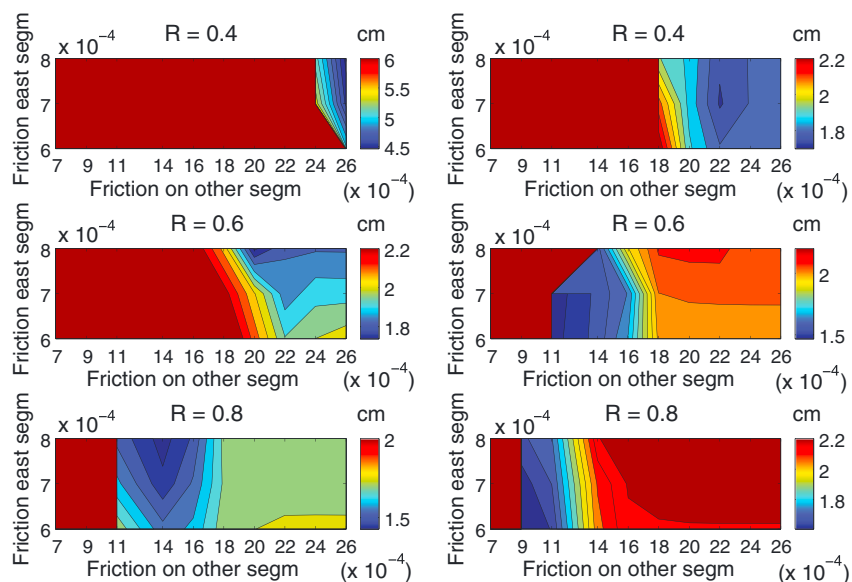

Figure 6. Variation of the WRMS misfit for the GPS data set. (left column) The result for an orientation of 50° and (right column) the result for an orientation of 60°. The y axis is the b friction constant on the eastern Léogâne segment, and the x axis is the b friction constant on the other segments where b is the constant from equation (4).
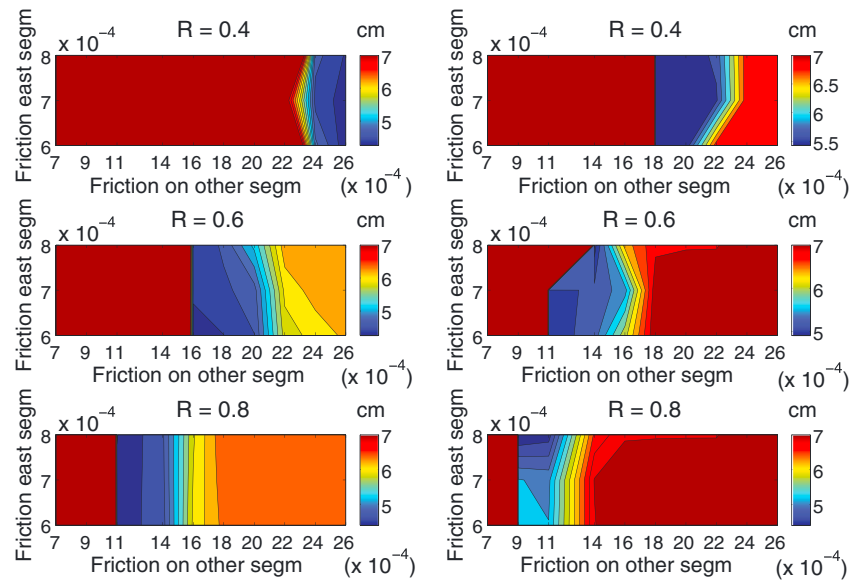
Figure 7. Variation of the WRMS misfit for the coral microatolls data set. (left column) The result for an orientation of 50° and (right column) the result for an orientation of 60°. The *y* axis is the *b* friction constant on the eastern Léogâne segment, and the *x* axis is the *b* friction constant on the other segments where *b* is the constant from equation (4).

assign to all faults a shear stress of 15 MPa, a normal stress of 100 MPa, a slip weakening distance (D_c) of 0.3 m, and static (μ_{static}) and dynamic ($\mu_{dynamic}$) friction coefficients of 0.3 and 0.04, respectively. We assume pure reverse shear traction on the eastern Léogâne and Trois Baies segments and pure left-lateral shear traction on the western Léogâne and Enriquillo segments.
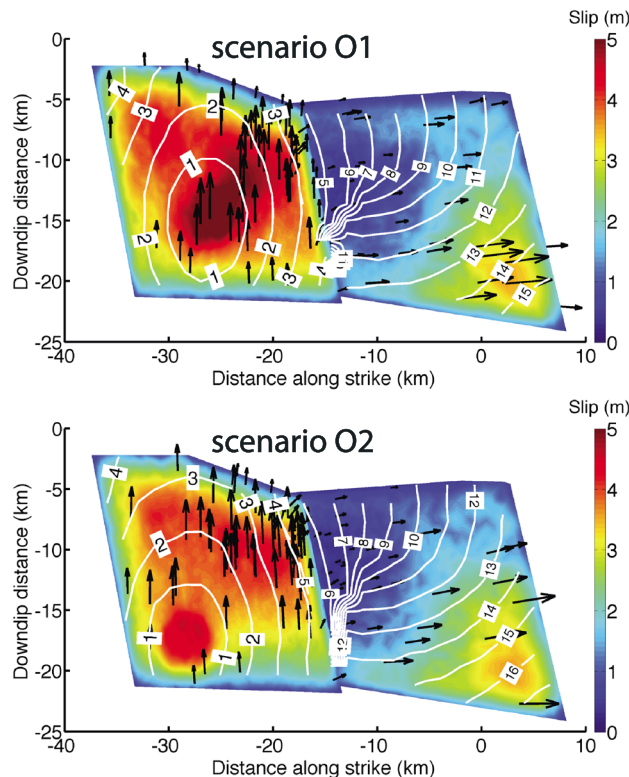
We initiate rupture at the center of the eastern Léogâne segment (scenario O1). We observe that it propagates across the entire eastern Léogâne segment and, after 3.5 s, transfers to the western Léogâne segment (Figure 8, top). We also observe that although the rupture criterion is reached very locally on the Enriquillo and the Trois Baies faults, the energy is not sufficient for a spontaneous rupture to develop on these two segments. These small perturbations are then dissipated very quickly.

We decreased the static friction on all faults in order to determine what would trigger slip on the Enriquillo or Trois Baies faults. We find that with a hypothesis of very weak faults with $\mu_{static} = 0.17$ (failure stress decreases from 30 MPa to 17 MPa) rupture transfers to all faults. Thus, the fact that the Enriquillo and the Trois Baies faults were not triggered during the 2010 Haiti earthquake was a function of the high strength
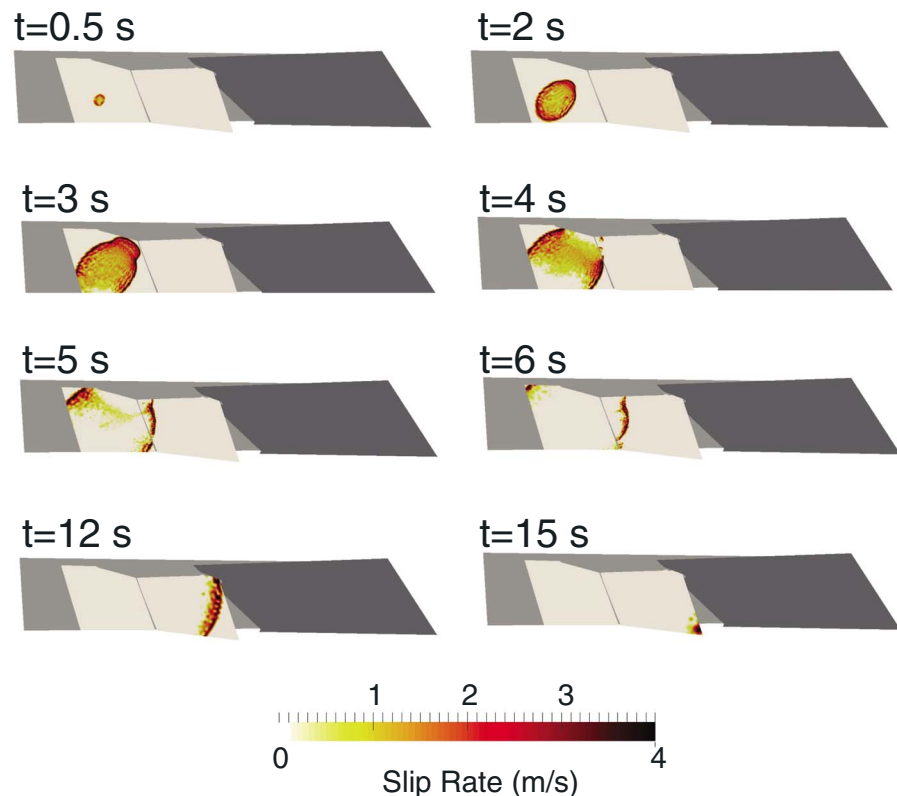

Figure 8. Distribution of final slip for scenarios (top) O1 and (bottom) O2. The colors denote the magnitude of the final slip. The arrows indicate the slip vectors at randomly selected point on the faults. The white lines indicate the rupture propagation, the time slip begins at each point on the faults.

Figure 9. Snapshot of rupture propagation on the fault for scenario C. For all three scenarios, the rupture on the eastern Léogâne is transferred on the western segment at about 3.5 s after nucleation.

of the faults combined with the geometry of the fault system and potentially the friction on those two faults.

We also ran a simulation shifting the nucleation zone to the bottom east corner of the eastern Léogâne segment (scenario O2), where rupture initiation is proposed by *Mercier de Lépinay et al.* [2011]. As the rupture front on the eastern Léogâne segment is unilateral over a longer distance than in scenario O1, the rupture should accumulate more energy and transfer to neighboring segments more easily. Results are, however, similar to scenario O1 (Figure 8, bottom), with increased slip at the initial crack location because of the larger stress drop. Rupture transfers to the western Léogâne segment after 4.5 s but not to the Enriquillo or Trois Baies faults.

As there is no seismological observation in the near field during the 2010 Haiti earthquake and we can only compare our simulation results with geodetic data of finite ground displacement, we cannot distinguish this difference in timing between scenario O1 and scenario O2 from the data. In the following, we therefore set rupture initiation to the center of the eastern Léogâne segment as in scenario O1.

4.2. Variable Stress Orientations

We now show simulation results that account for the known tectonic setting, as defined in the previous section (Figures 3 and 4 and Table 3), initiating nucleation at the same location as scenario O1 above. In all three scenarios (A, B, or C) the rupture breaks the whole eastern Léogâne segment and triggers the western segment after 3.5 s, but not the Enriquillo or Trois Baies faults (Figure 9).

As the rupture is propagating on the eastern Léogâne fault, the stress condition on the Enriquillo fault is changing (Figure 10). At 4 s two distinct patches of increase and decrease in shear stress develop on the Enriquillo fault. They continue to grow while the rupture is propagating on the western Léogâne fault. At the end, the simulation shows a significant increase in shear stress (Figure 10) at the top part of the Enriquillo fault (7 MPa) and to the west of the rupture (4 MPa). On the Trois Baies fault, shear stress increase is significant near its intersection with the Enriquillo fault and the western Léogâne fault, while the amplitude of the
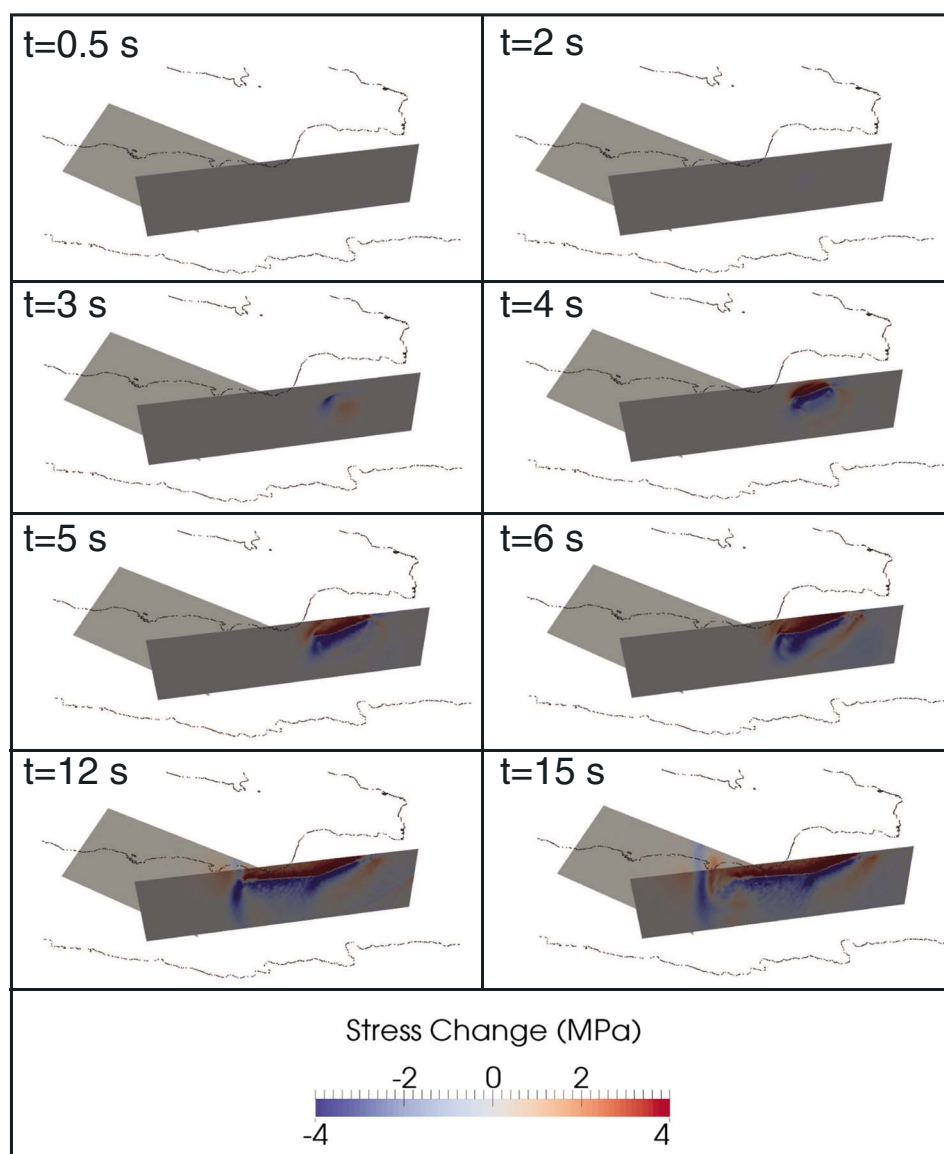
Figure 10. Snapshots of the shear stress change on the Enriquillo and Trois Baies faults for the scenario B. The shading indicates the magnitude of the shear stress change at different simulation times, and the dots indicate the coastlines.

stress change decreases with distance. Overall, the regions of increased and decreased shear stress on those two faults are consistent with the static coseismic Coulomb stress change from *Symithe et al.* [2013].

The final slip distribution bears similarities between scenarios A, B, and C (Figure 11). Simulations show mostly reverse slip on the eastern Léogâne segment, transitioning to strike slip on the western Léogâne segment. Maximum cumulative slip is about 5 m in the three scenarios, with most of the seismic moment released on the eastern Léogâne segment. We summarize the earthquake parameters obtained from the simulations in Table 4. This finite slip pattern and the total seismic moment release from all scenarios are consistent with several recent studies based on static-kinematic joint inversions of geodetic and/or seismological data [*Calais et al.*, 2010; *Hayes et al.*, 2010; *Meng et al.*, 2012; *Symithe et al.*, 2013]. The temporal evolution of the moment rate (Figure 12) shows two peaks separated by about 8 s, the first one more impulsive, consistent with the source time function derived from seismological data by *Meng et al.* [2012].

Although the cumulative moment release is similar for all three scenarios (corresponding to $M_w 7.1$), there are some differences in the detail of the rupture process. Scenarios A and B generate more slip on the western Léogâne segment than the eastern one, while the opposite is obtained for scenario C. This is
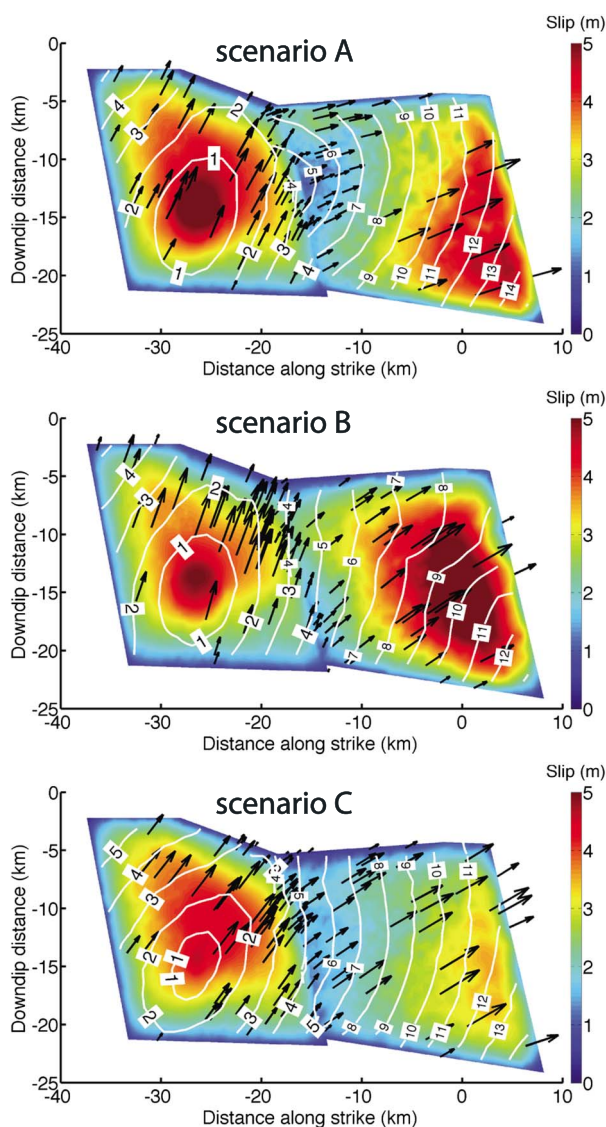
Figure 11. Distribution of final slip distribution for scenarios A, B and C for the dynamic model with regional tectonic stress field resolved onto all fault segments. The arrows indicate the slip vectors at randomly selected finite elements. The white lines indicate the rupture propagation, the time slip begins at each point on the faults. Scenario A displays a faster rupture propagation, and slower propagation is shown in scenario B.

because static stress drop on the western segment is significantly larger in scenarios A and B (15.8 MPa and 12.2 MPa, respectively) than in scenario C (10.3 MPa). Also, scenarios A and B are more impulsive than scenario C at the start. The reason for that is although the shear stress magnitudes for all three scenarios are of the same order, the updip component of the shear stress on the eastern Léogâne is higher for scenarios A and B compare to scenario C.

All three scenarios show strike-slip motion with some component of reverse dip-slip motion on the western part of the Léogâne fault rather than purely strike-slip motion as reported in previous studies [*Calais et al.*, 2010; *Hayes et al.*, 2010; *Symithe et al.*, 2013]. The reason for this difference is due to the trade-off in the chosen azimuth of the maximum principal stress (Figure 3). A smaller value (less than 50°) would generate more strike-slip motion on the western segment but less dip-slip motion on the eastern segment of the Léogâne fault. On the other hand, a larger azimuth (more than 50°) would generate less strike-slip motion on the western segment but more dip-slip motion on the eastern segment of the Léogâne fault.

4.3. Comparison With Observed Surface Deformation

Although the simulations described above produce a rupture propagating from the eastern to the western Léogâne segments with a similar pattern, they result in different deformation of the ground surface. To score each scenario we compare the final surface displacements from the simulations to the coseismic observations from GPS, InSAR, and coastal uplifts from coral microatolls (Figure 13). Overall, the fit is remarkably good for all three scenarios, considering that these are forward models based on fairly simple mechanical assumptions. Scenario C has the smallest weighted RMS misfit of the three and matches the geodetic observations as well

Table 4. Summary of Earthquake Rupture

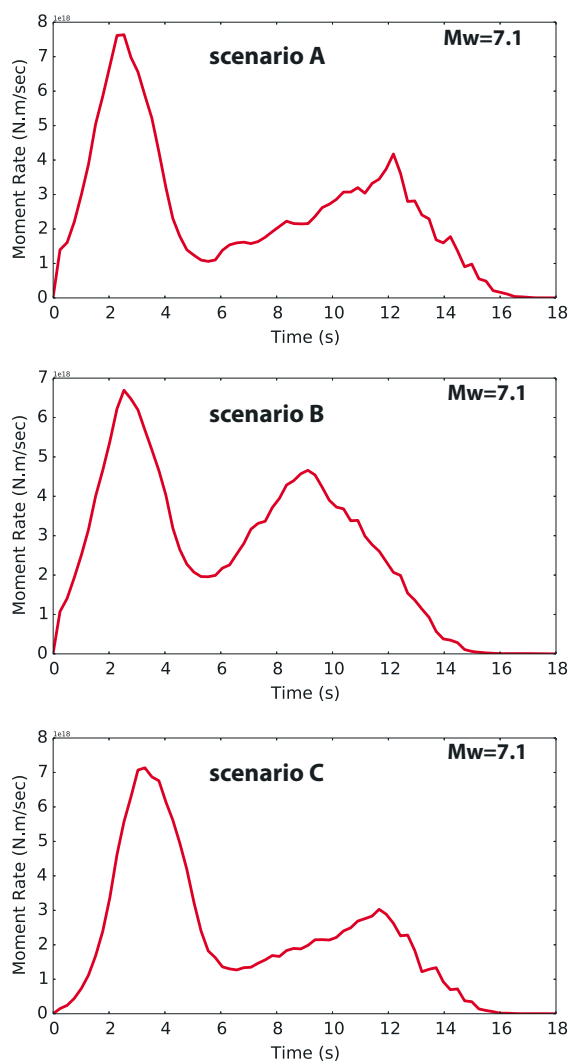| Scenario	Mo (N m)	M_w	East Léogâne			West Léogâne		
			Mo (N m)	Average Slip (m)	Average Rake	Mo (N m)	Average Slip (m)	Average Rake
A	5.64E+19	7.1	2.77E+19	2.96	58°	2.87E+19	2.75	sd18°
B	5.80E+19	7.1	2.50E+19	2.66	68°	3.30E+19	3.16	33°
C	4.94E+19	7.1	2.65E+19	2.83	49°	2.29E+19	2.19	30°

Figure 12. Moment rate function with respect to time for all three scenarios. All three scenarios have a moment magnitude of 7.1. The moment rate function for each scenario indicates two prominent peak at about 8 s apart which is consistent with the source time function from *Meng et al.* [2012].

as the published kinematic finite source inversions [*Calais et al.*, 2010; *Hayes et al.*, 2010; *Meng et al.*, 2012; *Symithe et al.*, 2013].

In the process of comparing simulation outputs to InSAR displacements, we also tested the exact same Léogâne fault geometry as used by *Symithe et al.* [2013] in their finite fault inversion of geodetic data. As also noted in their paper, this results in a systematic offset of 1.5–3 km between the observed and simulated interferograms. *Symithe et al.* [2013] propose that this offset results from the 1-D seismic velocity model used by *Douilly et al.* [2013] in their after-shock relocations. These authors allow for the possibility of a bias up to 1–2 km southward based on systematic traveltime residuals for a few stations in the south-ern part of the southern peninsula. The geometry chosen here, where the Léogâne fault is located 2 km to the north compared to *Symithe et al.* [2013] and scenario C is assumed, shows a very good agreement with the vertical coseismic motion from InSAR (Figure 14), with a weighted RMS misfit to 0.035 m. We therefore suggest that further work on this earthquake assumes the geometry used in this study best fit dynamic model.

5. Discussion
5.1. Implications for Fault Interactions
The dynamic simulations described above show that the rupture of the 2010 Haiti earthquake can be reproduced successfully using a simple geometry (Léogâne divided into two segments) and simple assumptions about the model parameters. A key f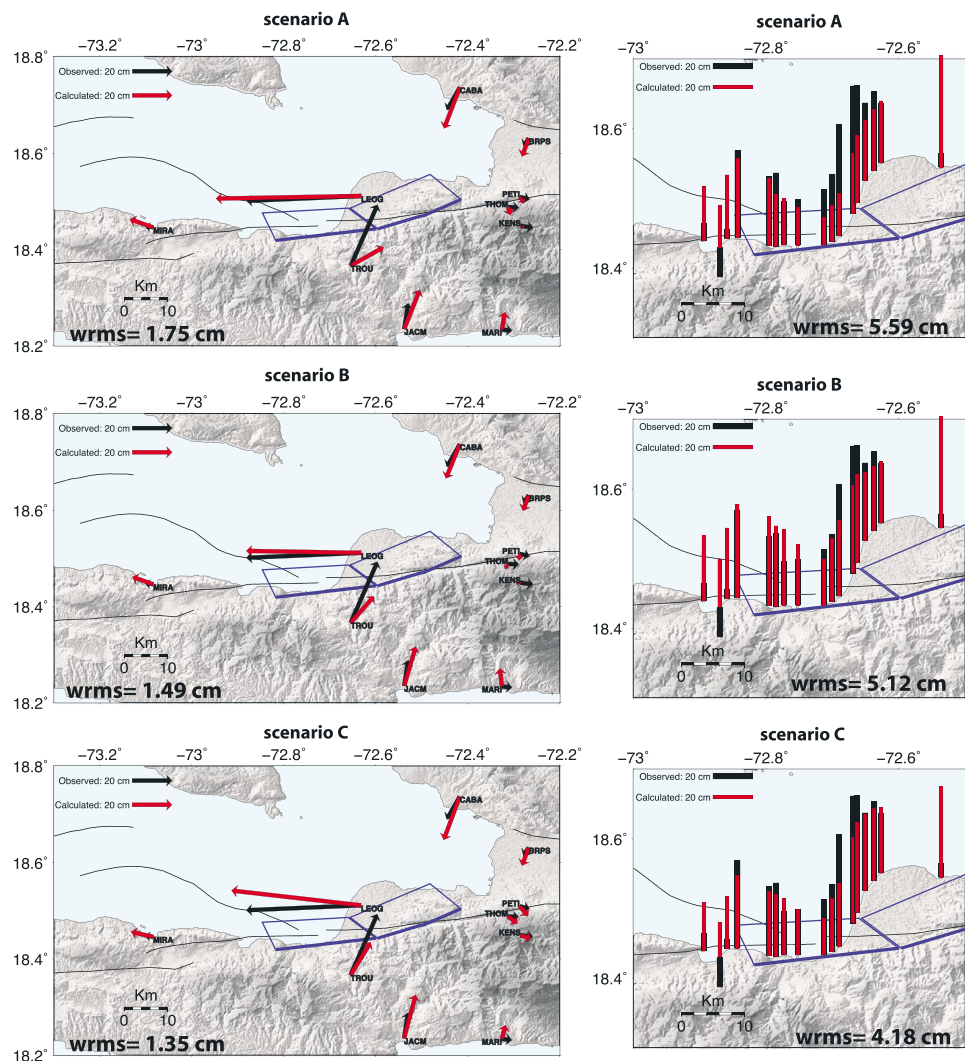eature of these successful simulations is the fact that the Enriquillo and Trois Baies faults are not triggered by the earthquake (for both the homogeneous and heterogeneous stress field cases), in spite of significant dynamic stress changes imparted by the rupture as shown in Figure 15.

Figure 15 shows the evolution of slip, slip rate, and shear stress magnitude with time on specific point on each fault as shown in Figure 2. By initiating the rupture on the eastern Léogâne segment and due to the chosen frictional parameters and slip weakening distance, the shear stress on the point on that segment starts increasing at 2.8 s and slip begins at 3 s. Because of the small distance to failure value ($\tau_f - \tau_i$) com-pared to the dynamic stress drop ($\tau_i - \tau_s$) and since we initiate the rupture on this fault, the rupture is able to propagate along the entire segment. If we increase the slip weakening distance, then the rupture slows down and eventually stops within the eastern Léogâne segment without impacting other model faults.

At about 3.5 s, the rupture reaches the intersection between the two segments and at 8.5 s shear stress starts increasing on the point on the western segment. Failure stress on that segment is higher than on the eastern one, but the shear stress imparted by the rupture to the east eventually overcomes the failure stress, triggering slip at about 10 s. The reason for this significant increase in shear stress at the intersection between the two segments is the favorable orientation of the western segment with respect to the stress

Figure 13. (left column) The observed (GPS) and calculated horizontal displacement for each scenario. (right column) The observed (coastal uplift) and calculated vertical displacements for each scenario. The blue lines indicate the surface projection of the two segments of the Léogâne fault, and the thicker blue line indicates the top part of the fault.

changes imparted by rupture propagation on the eastern segment, a result consistent with previous studies on branched fault system [*Aochi et al.*, 2000a, 2000b, 2002; *Harris et al.*, 2002; *Oglesby et al.*, 2003; *Kame et al.*, 2003; *Aochi et al.*, 2005; *Duan and Oglesby*, 2005].

The dynamic stress perturbation reaches the Enriquillo and the Trois Baies faults at about 4 and 12.5 s, respectively. The regional stress regime and the strike and dip of those faults are such that the increase in stress (5 MPa and 3 MPa, respectively) are insufficient to overcome failure stress and trigger slip. This also is consistent with *Aochi et al.* [2000a], who find that rupture propagation among branch faults strongly depends on the angle between the faults and the preloaded stress among them. For this event, the lack of rupture of the Enriquillo fault can be explained by the low angle between it and the east Léogâne fault and by the friction parameters applied to them. In our investigation of the parameters for the dynamic rupture, we showed that a decrease of the static friction would allow the rupture to jump on the Enriquillo fault. However, this would result in a total misfit with the surface observation and a seismic moment which does not agree with previous studies.

Nevertheless, the rupture transfer from one segment to another strongly depends on the geometry of the fault segments and on the stress and frictional condition given on each segment [e.g., *Harris et al.*, 1991,
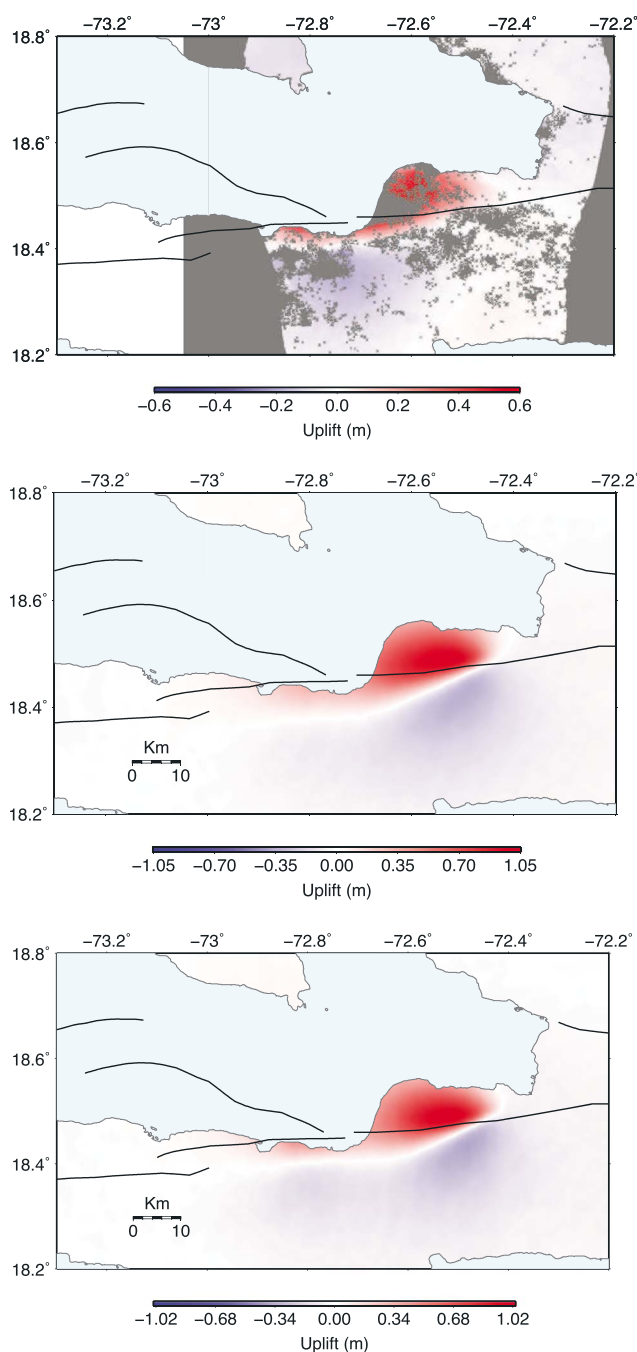
Figure 14. (top) The uplift component for the InSAR data from *Hayes et al.* [2010]. (middle) The calculated vertical displacement for a dynamic rupture on the fault geometry from *Symithe et al.* [2013]. (bottom) The calculated vertical displacement from our best simulation. There is a systematic shift of about 2 km to the south in the uplift component from *Symithe et al.* [2013] model which does not fit the vertical InSAR component from *Hayes et al.* [2010].

2002; *Harris and Day*, 1993, 1999; *Aochi et al.*, 2000a, 2002, 2006, 2003; *Oglesby*, 2005]. In our simulations, the rupture propagates onto all the model segments if we suppose very weak faults ($\mu_{static} = 0.17$). In other words, the simulation results support the notion that the fault strength should not be that low, which is consistent with the other dynamic rupture simulations of similar segmentation situations [*Harris et al.*, 2002]. The rupture transfer is also controlled by the geometrical irregularities between the segments such as gap distance [e.g., *Harris et al.*, 1991]. *Kase* [2010] showed that the rupture transfer becomes more difficult from the second to third segment than the first to the second, as the propagating rupture cannot keep sufficient energy to rupture distant fault segment. With a similar analogy, if the medium between the segments behaves anelastically for a large deformation [*Geist and Andrews*, 2000], it may absorb a significant amount of rupture energy, which in turn hinders rupture transfer to neighboring segments. All these factors act to prevent rupture transfer from the western Léogâne segment to the other fault segments and thus do not change our general conclusion. Another important aspect of our simulations is the requirement to parameterize the eastern Léogâne segment as weaker than the neighboring segments in order to insure westward rupture propagation even though other studies stated that the fault strength is also depending on the maturity of the fault [*Manighetti et al.*, 2007]. The presence of water and a variation of the fault roughness [*Byerlee*, 1978] might be a possible explanation for this difference in fault friction. Unfortunately, there is no independent information on fault rheology in southern Haiti. 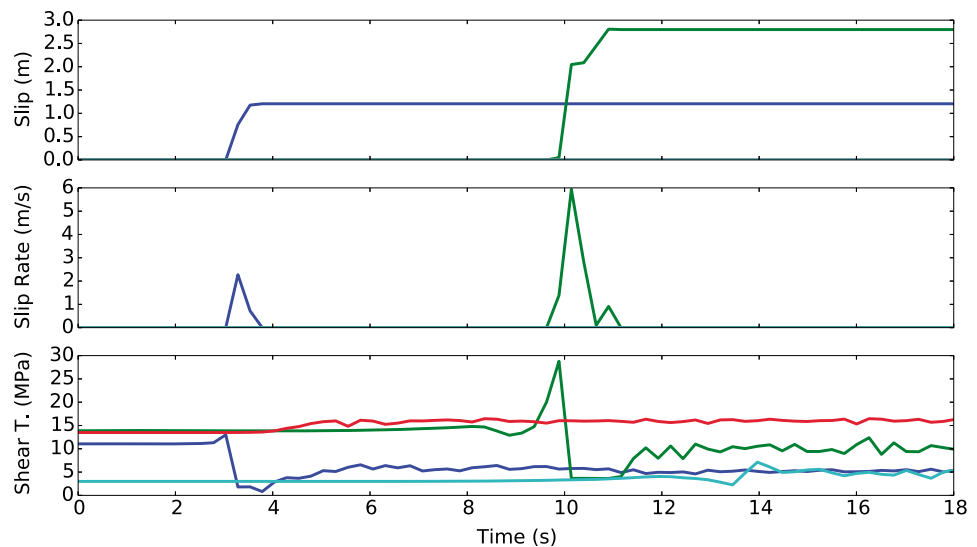Further investigations, perhaps from geodynamic modeling and seismological observations, is needed to better understand both the ambient state of stress and fault rheology.

5.2. Ground Motion in the Near Field
Although there was no near-field seismic station to record the 2010 Haiti earthquake, *Mavroeidis and Scotti* [2013] used the multifault slip model from *Hayes et al.* [2010]—quite different from the geometry

Figure 15. Slip, slip rate, and shear stress time histories for locations on the eastern Léogâne (blue line), western Léogâne (green line), Enriquillo (red line), and Trois Baies fault (cyan line) from scenario C. The location of those points are shown in Figure 2. For the point on the eastern Léogâne segment, the shear stress starts increasing at 2.8 s and slip starts at 3 s. For the corresponding point on the western Léogâne segment, slip occurs at 10 s. Although rupture does not propagate to the Enriquillo and the Trois Baies faults, significant stress change magnitude has been observed on those two faults.

used here—and the discrete wave number method [*Bouchon and Aki*, 1977; *Bouchon*, 1979] to compute low-frequency (1 Hz) synthetic seismograms at several sites in the epicentral region (Table 5 and Figure 1). They argue that westward rupture directivity should have led to significantly larger ground motion at stations PGv and PRY located to the west of the rupture than at PaP (Port-au-Prince) located to the east. Their calculations are, however, based on a kinematic rupture model.

Here we extract ground displacement and velocity on the ground surface from our best fit dynamic rupture model (scenario C). The highest frequency in our simulation is 2.3 Hz; we therefore low-pass filter our synthetic seismograms to 1 Hz to compare with those from *Mavroeidis and Scotti* [2013]. In both cases the origin of the time histories coincides with the rupture nucleation at their respective hypocenters (Figure 16). For the two stations (PGv and PRY) located to the west of the rupture zone, the synthetics from the dynamic rupture match well those calculated by *Mavroeidis and Scotti* [2013] in spite of a very different rupture geometry. The seismograms are characterized by a dominant pulse mostly in the NS component (visible in velocity and displacement). This is because these two sites are sufficiently far from the ruptured area so that the detailed difference in fault geometry does not significantly impact the waveforms. The discrepancy is more visible for stations FUC, LaC, and LEO located near the rupture area: the vertical motions are well replicated but the peak horizontal motions (except the N-S component for LEO) are of opposite sign. Since *Hayes et al.* [2010] inferred the slip on the south dipping Enriquillo fault, this discrepancy might be due to the contribution of this fault as shown in Figure 4 in *Mavroeidis and Scotti* [2013]. The Port-au-Prince (PaP) station shows a fairly large velocity pulse, much larger than *Mavroeidis and Scotti* [2013]'s results. This is because 70% of the moment release in the finite fault model of *Hayes et al.* [2010] occurred on the north dipping segment in their model. As a result, fault-to-station distance is greater than in our study, resulting in a smaller velocity pulse. The good overall agreement between the two studies indicates that the dynamic rupture simulations could provide good estimates of peak ground motion in this region.

We also calculated ground acceleration at the selected stations using the central difference method (in Figure 16, third
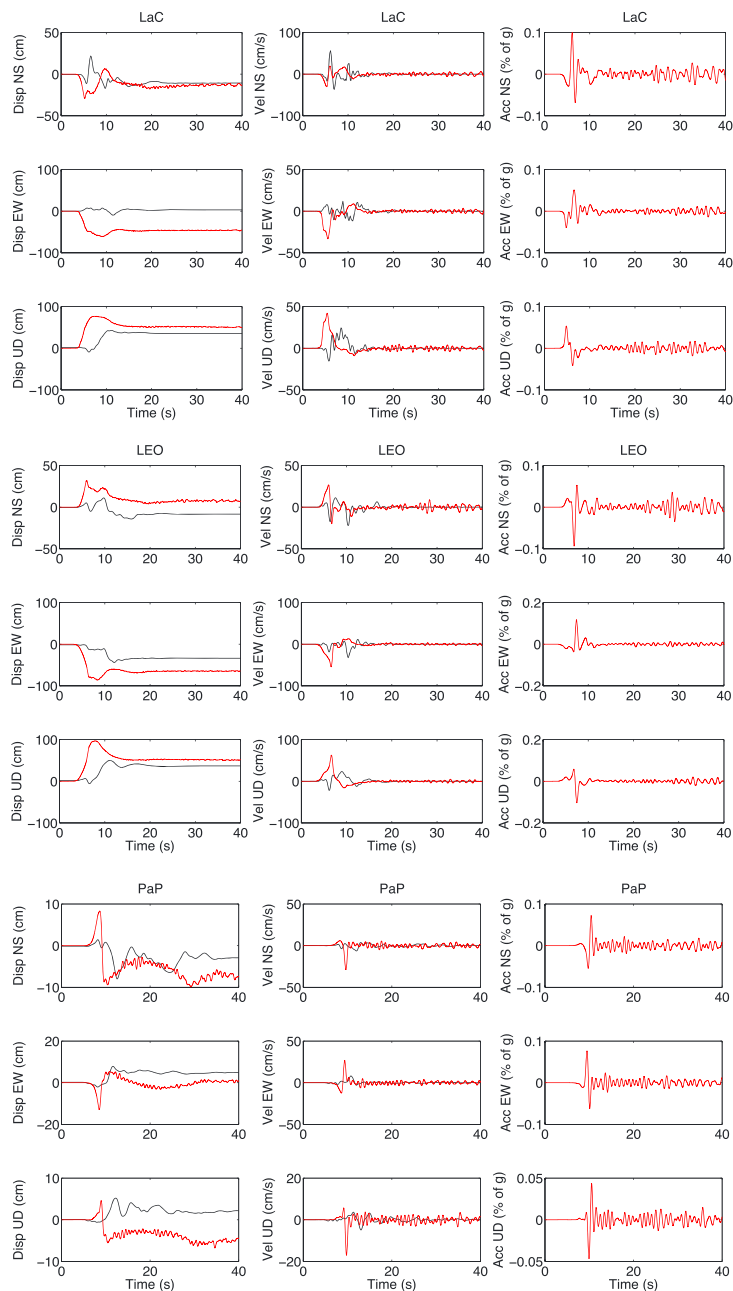
Table 5. Sites Selected for Low-Frequency Ground Motion

Site Name	Site Abbreviation	Latitude (°)	Longitude (°)
Fouche	FUC	N18.4217	W72.7342
L'acul	LaC	N18.4498	W72.6692
Léogâne	LEO	N18.5107	W72.6336
Port-au-Prince	PaP	N18.5389	W72.3358
Petit Goâve	PGv	N18.4337	W72.8613
Port Royal	PRY	N18.4370	W72.9057
Trois Palmiste	TPM	N18.3478	W72.6519

Figure 16. Synthetic seismograms filtered to 1 Hz showing the displacement (first column), velocity (second column), and acceleration time histories (third column) for seven selected sites near the rupture area. The red lines are the results from scenario C of dynamic rupture simulation, and the black lines are the results from *Mavroeidis and Scotti* [2013] which used the slip model from *Hayes et al.* [2010] and a discrete wave number method to generate the deformation at the surface.

column). We had to filter the acceleration in order to reduce numerical noises in the signal which was generating some bias in the amplitudes of the ground motion. Since there is no strong motion record for this event, we compare our results to the synthetic acceleration from *Mavroeidis and Scotti* [2013], the peak ground acceleration (PGA) from the USGS shake map, and the results from the Next Generation Attenuation ground motion prediction equations (GMPEs) [*Green et al.*, 2011; *Olson et al.*, 2011]. The PGA values generated from our dynamic rupture model for stations located near the rupture area (FUC, LaC, and LEO) are ∼0.1 g, considerably smaller than the other studies. *Olson et al.* [2011] estimated a PGA of 0.48 g at FUC and 0.42 g at LaC. The USGS shake map indicates a PGA of 0.4 g at FUC, 0.47 g at LaC, and 0.51 g at LEO.
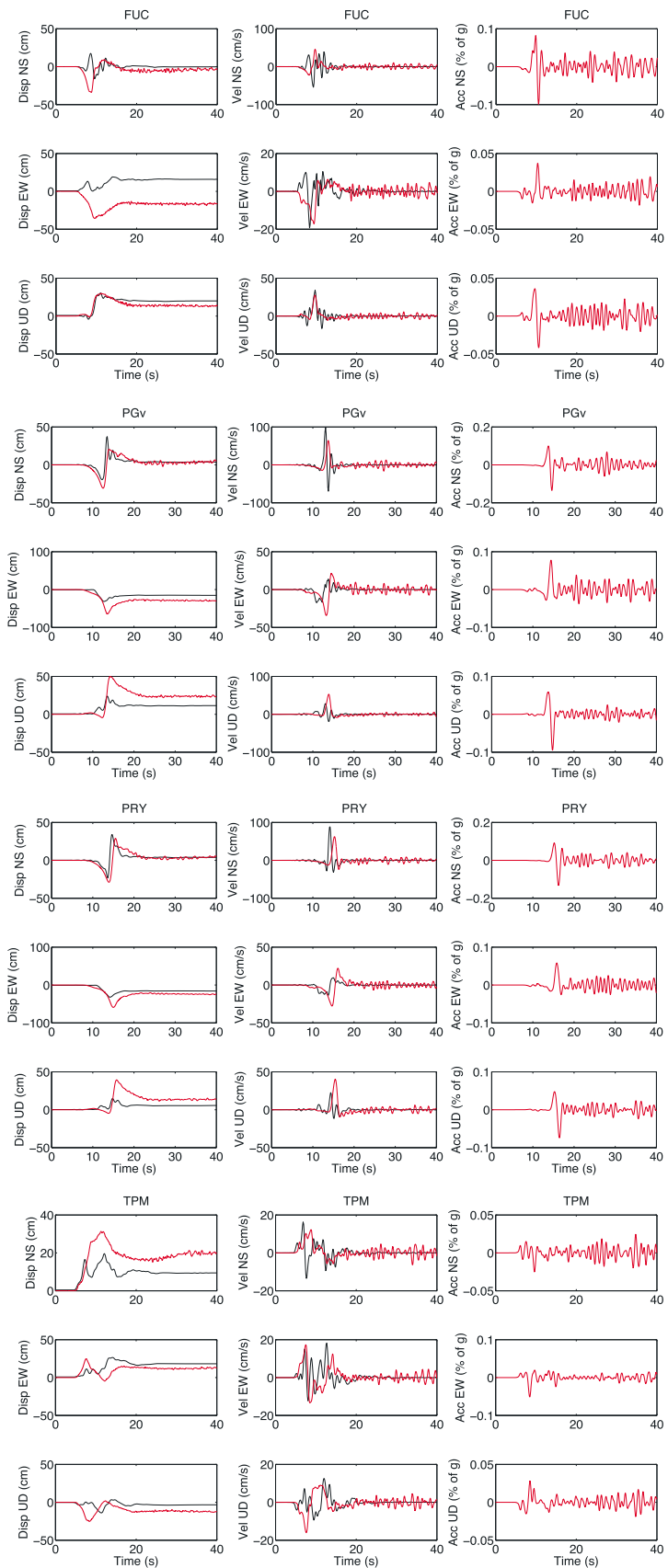
Figure 16. (continued)

The simulated PGA at LEO from *Mavroeidis and Scotti* [2013] agrees with *Olson et al.* [2011], however, their estimates for LaC and FUC are slightly greater (~0.6 g).

For stations farther away from the rupture area, we find a PGA of (~0.15 g) for PRY and PGv and less than 0.1 g for TPM which are still significantly lower than the other studies. In Port-au-Prince, our estimate of ~0.1 g is close to that of *Hough et al.* [2012], who used a rigid body displacement method to estimate a PGA of ~0.2 g, significantly lower than those reported by *Mavroeidis and Scotti* [2013], *Olson et al.* [2011], and the USGS shake map, where PGA is ~0.3 g. The reason for this discrepancy is because PGA is usually controlled by high frequencies which our models could not generate since the highest frequency of the mesh is 2.3 Hz, and we had to filter the ground acceleration in order to reduce the digital noises. Also, these generated synthetics do not take into account any site effects, which have been shown to be important in Port-au-Prince in particular [*Hough et al.*, 2010, 2011], but are not considered in our modeling. For better understanding the ground motions and the disaster in the Port-au-Prince area, it will be necessary to combine the reliable input ground motions estimated from the deterministic simulations of this study and the site amplification effect inferred in the ongoing microzonation study [*Gilles et al.*, 2013].

6. Conclusions

The dynamic rupture simulations of the 2010, M_w7.0, Haiti earthquake described here show that a simple two-segment, planar fault geometry derived from the precise aftershock relocation study of *Douilly et al.* [2013], together with the appropriate regional stress and friction model, can successfully replicate a rupture propagating from east to west and a finite ground displacement consistent with geodetic observations. PGA estimates in the near- and far-field area are lower than other studies, but this is probably because local site conditions were not included in our larger-scale models.

This physically sound model calculated here agrees well with finite fault inversions of geodetic and seismological observations. The two fault patches inferred in most finite fault inversions can be explained by the successive rupture of two fault segments oriented favorably with respect to the rupture propagation in the presence of appropriate tectonic stresses, friction coefficients, and slip weakening distance to those faults.

As inferred from finite fault inversions, rupture does not propagate to the neighboring Enriquillo or Trois Baies faults because, given their geometry and orientation (strike and dip) with respect to the rupture propagation on the Léogâne fault, shear stress on those two faults did not reach failure. However, simulations indicate a significant static stress increase on the top and to the west of the Enriquillo fault and also on the Trois Baies fault near its intersection to the Enriquillo and the western Léogâne segment, consistent with previous results from finite fault inversions [*Symithe et al.*, 2013]. This should serve as a reminder that the Enriquillo fault remains a major threat for southern Haiti.

The 1989 Loma Prieta earthquake and the San Andreas fault, and the 2010 Haiti earthquake and the Enriquillo fault are examples of where rupture initiation on a secondary thrust did not trigger the main plate boundary fault. This may also be the case of the 1701 M_I6.6 and 1751 M_I6.6, and 1860 M_I 6.3 events in southern Haiti [*Bakun et al.*, 2012]. In a complex plate boundary zone, it is possible that more small, secondary faults are favorably oriented to be triggered than major plate boundary faults. Small events on the former should then be more frequent—hence more likely to be captured in the historical record—than large earthquakes on the major faults.

References

Aagaard, B., S. Kientz, M. Knepley, S. Somala, L. Strand, and C. Williams (2013a), *Pylith user manual, version 1.9.0.* Computational Infrastructure for Geodynamics (CIG), Univ. of California, Davis. [Available at http://www.geodynamics.org/cig/software/pylith/pylith-manual.pdf.]

Aagaard, B., M. Knepley, and C. Williams (2013b), A domain decomposition approach to implementing fault slip in finite-element models of quasi-static and dynamic crustal deformation, *J. Geophys. Res. Solid Earth*, *118*, 3059–3079, doi:10.1002/jgrb.50217.

Aagaard, B. T., T. H. Heaton, and J. F. Hall (2001), Dynamic earthquake ruptures in the presence of lithostatic normal stresses: Implications for friction models and heat production, *Bull. Seismol. Soc. Am.*, *91*(6), 1765–1796.

Aagaard, B. T., G. Anderson, and K. W. Hudnut (2004), Dynamic rupture modeling of the transition from thrust to strike-slip motion in the 2002 Denali fault earthquake, Alaska, *Bull. Seismol. Soc. Am.*, *94*(6B), S190–S201.

Andrews, D. (1976), Rupture velocity of plane strain shear cracks, *J. Geophys. Res.*, *81*(32), 5679–5687.

Angelier, J. (1979), Determination of the mean principal directions of stresses for a given fault population, *Tectonophysics*, *56*(3), T17–T26.

Angelier, J. (1990), Inversion of field data in fault tectonics to obtain the regional stress—III. A new rapid direct inversion method by analytical means, *Geophys. J. Int.*, *103*(2), 363–376.

Aochi, H., E. Fukuyama, and M. Matsu'ura (2000a), Selectivity of spontaneous rupture propagation on a branched fault, *Geophys. Res. Lett.*, *27*(22), 3635–3638.

Aochi, H., E. Fukuyama, and M. Matsu'ura (2000b), Spontaneous rupture propagation on a non-planar fault in 3-D elastic medium, *Pure Appl. Geophys.*, *157*(11–12), 2003–2027.

Aochi, H., R. Madariaga, and E. Fukuyama (2002), Effect of normal stress during rupture propagation along nonplanar faults, *J. Geophys. Res.*, *107*(B2), 2038, doi:10.1029/2001JB000500.

Aochi, H., R. Madariaga, and E. Fukuyama (2003), Constraint of fault parameters inferred from nonplanar fault modeling, *Geochem. Geophys. Geosyst.*, *4*(2), 1020, doi:10.1029/2001GC000207.

Aochi, H., O. Scotti, and C. Berge-Thierry (2005), Dynamic transfer of rupture across differently oriented segments in a complex 3-D fault system, *Geophys. Res. Lett.*, *32*, L21304, doi:10.1029/2005GL024158.

Aochi, H., M. Cushing, O. Scotti, and C. Berge-Thierry (2006), Estimating rupture scenario likelihood based on dynamic rupture simulations: The example of the segmented Middle Durance fault, southeastern France, *Geophys. J. Int.*, *165*(2), 436–446.

Bakun, W., C. Flores, and S. Uri (2012), Significant earthquakes on the Enriquillo fault system, Hispaniola, 1500–2010: Implications for seismic hazard, *Bull. Seismol. Soc. Am.*, *102*(1), 18–30.

Beavan, J., M. Motagh, E. J. Fielding, N. Donnelly, and D. Collett (2012), Fault slip models of the 2010–2011 Canterbury, New Zealand, earthquakes from geodetic data and observations of postseismic ground deformation, *N. Z. J. Geol. Geophys.*, *55*(3), 207–221.

Benford, B., C. DeMets, and E. Calais (2012), Gps estimates of microplate motions, Northern Caribbean: Evidence for a hispaniola microplate and implications for earthquake hazard, *Geophys. J. Int.*, *191*(2), 481–490.

Beroza, G. C. (1991), Near-source modeling of the Loma Prieta earthquake: Evidence for heterogeneous slip and implications for earthquake hazard, *Bull. Seismol. Soc. Am.*, *81*(5), 1603–1621.

Bouchon, M. (1979), Discrete wave number representation of elastic wave fields in three-space dimensions, *J. Geophys. Res.*, *84*(B7), 3609–3614.

Bouchon, M., and K. Aki (1977), Discrete wave-number representation of seismic-source wave fields, *Bull. Seismol. Soc. Am.*, *67*(2), 259–277.

Byerlee, J. (1978), Friction of rocks, *Pure Appl. Geophys.*, *116*(4–5), 615–626.

Calais, E., Y. Mazabraud, B. Mercier de Lépinay, P. Mann, G. Mattioli, and P. Jansma (2002), Strain partitioning and fault slip rates in the Northeastern Caribbean from GPS measurements, *Geophys. Res. Lett.*, *29*(18), 1856, doi:10.1029/2002GL015397.

Calais, E., et al. (2010), Transpressional rupture of an unmapped fault during the 2010 Haiti earthquake, *Nat. Geosci.*, *3*(11), 794–799.

Das, S., and K. Aki (1977), A numerical study of two-dimensional spontaneous rupture propagation, *Geophys. J. R. Astron. Soc.*, *50*(3), 643–668.

Day, S. M. (1982), Three-dimensional simulation of spontaneous rupture: The effect of nonuniform prestress, *Bull. Seismol. Soc. Am.*, *72*(6A), 1881–1902.

DeMets, C., P. Jansma, G. S. Mattioli, T. H. Dixon, F. Farina, R. Bilham, E. Calais, and P. Mann (2000), GPS geodetic constraints on Caribbean-North America plate motion, *Geophys. Res. Lett.*, *27*(3), 437–440.

Dietz, L. D., and W. L. Ellsworth (1990), The October 17, 1989, Loma Prieta, California, earthquake and its aftershocks: Geometry of the sequence from high-resolution locations, *Geophys. Res. Lett.*, *17*(9), 1417–1420.

Douilly, R., et al. (2013), Crustal structure and fault geometry of the 2010 Haiti earthquake from temporary seismometer deployments, *Bull. Seismol. Soc. Am.*, *103*(4), 2305–2325.

Duan, B., and D. D. Oglesby (2005), Multicycle dynamics of nonplanar strike-slip faults, *J. Geophys. Res.*, *110*, B03304, doi:10.1029/2004JB003298.

Eberhart-Phillips, D., et al. (2003), The 2002 Denali fault earthquake, Alaska: A large magnitude, slip-partitioned event, *Science*, *300*(5622), 1113–1118.

Geist, E. L., and D. Andrews (2000), Slip rates on San Francisco Bay area faults from anelastic deformation of the continental lithosphere, *J. Geophys. Res.*, *105*(B11), 25,543–25,552.

Gephart, J. W., and D. W. Forsyth (1984), An improved method for determining the regional stress tensor using earthquake focal mechanism data: Application to the San Fernando earthquake sequence, *J. Geophys. Res.*, *89*(B11), 9305–9320.

Gilles, R., D. Bertil, M. Belvaux, A. Roulle, G. Noury, C. Prepetit, and J. Jean-Philippe (2013), Seismic microzoning in the metropolitan area of Port-au-Prince-complexity of the subsoil, Abstract S51A-2312 presented at 2013 Fall Meeting, AGU, San Francisco, Calif.

Gledhill, K., J. Ristau, M. Reyners, B. Fry, and C. Holden (2011), The Darfield (Canterbury, New Zealand) Mw 7.1 earthquake of September 2010: A preliminary seismological report, *Seismol. Res. Lett.*, *82*(3), 378–386.

Green, R. A., S. M. Olson, B. R. Cox, G. J. Rix, E. Rathje, J. Bachhuber, J. French, S. Lasley, and N. Martin (2011), Geotechnical aspects of failures at Port-au-Prince seaport during the 12 January 2010 Haiti earthquake, *Earthquake Spectra*, *27*(S1), S43–S65.

Hardebeck, J. L., and A. J. Michael (2006), Damped regional-scale stress inversions: Methodology and examples for southern California and the Coalinga aftershock sequence, *J. Geophys. Res.*, *111*, B11310, doi:10.1029/2005JB004144.

Harris, R., et al. (2009), The SCEC/USGS dynamic earthquake rupture code verification exercise, *Seismol. Res. Lett.*, *80*(1), 119–126.

Harris, R. A., and S. M. Day (1993), Dynamics of fault interaction: Parallel strike-slip faults, *J. Geophys. Res.*, *98*(B3), 4461–4472.

Harris, R. A., and S. M. Day (1999), Dynamic 3D simulations of earthquakes on en echelon faults, *Geophys. Res. Lett.*, *26*(14), 2089–2092.

Harris, R. A., R. J. Archuleta, and S. M. Day (1991), Fault steps and the dynamic rupture process: 2-D numerical simulations of a spontaneously propagating shear fracture, *Geophys. Res. Lett.*, *18*(5), 893–896.

Harris, R. A., J. F. Dolan, R. Hartleb, and S. M. Day (2002), The 1999 Izmit, Turkey, earthquake: A 3D dynamic stress transfer model of intraearthquake triggering, *Bull. Seismol. Soc. Am.*, *92*(1), 245–255.

Hayes, G., et al. (2010), Complex rupture during the 12 January 2010 Haiti earthquake, *Nat. Geosci.*, *3*(11), 800–805.

Hough, S. E., et al. (2010), Localized damage caused by topographic amplification during the 2010 m 7.0 Haiti earthquake, *Nat. Geosci.*, *3*(11), 778–782.

Hough, S. E., A. Yong, J. R. Altidor, D. Anglade, D. Given, and S.-L. Mildor (2011), Site characterization and site response in Port-au-Prince, Haiti, *Earthquake Spectra*, *27*(S1), S137–S155.

Hough, S. E., T. Taniguchi, and J.-R. Altidor (2012), Estimation of peak ground acceleration from horizontal rigid body displacement: A case study in Port-au-Prince, Haiti, *Bull. Seismol. Soc. Am.*, *102*(6), 2704–2713.

Hreinsdóttir, S., J. T. Freymueller, R. Bürgmann, and J. Mitchell (2006), Coseismic deformation of the 2002 Denali fault earthquake: Insights from GPS measurements, *J. Geophys. Res.*, *111*, B03308, doi:10.1029/2005JB003676.

Hunter, J. D. (2007), Matplotlib: A 2D graphics environment, *Comput. Sci. Eng.*, *9*(3), 0090–95.

Ida, Y. (1972), Cohesive force across the tip of a longitudinal-shear crack and Griffith's specific surface energy, *J. Geophys. Res.*, *77*(20), 3796–3805.

Kame, N., J. R. Rice, and R. Dmowska (2003), Effects of prestress state and rupture velocity on dynamic fault branching, *J. Geophys. Res.*, *108*(B5), 2265, doi:10.1029/2002JB002189.

Kase, Y. (2010), Slip-length scaling law for strike-slip multiple segment earthquakes based on dynamic rupture simulations, *Bull. Seismol. Soc. Am.*, *100*(2), 473–481.

Kilb, D., M. Ellis, J. Gomberg, and S. Davis (1997), On the origin of diverse aftershock mechanisms following the 1989 Loma Prieta earthquake, *Geophys. J. Int.*, *128*(3), 557–570.

Madariaga, R., K. Olsen, and R. Archuleta (1998), Modeling dynamic rupture in a 3D earthquake fault model, *Bull. Seismol. Soc. Am.*, *88*(5), 1182–1197.

Manaker, D. M., E. Calais, A. Freed, S. Ali, P. Przybylski, G. Mattioli, P. Jansma, C. Prépetit, and J. De Chabalier (2008), Interseismic plate coupling and strain partitioning in the Northeastern Caribbean, *Geophys. J. Int.*, *174*(3), 889–903.

Manighetti, I., M. Campillo, S. Bouley, and F. Cotton (2007), Earthquake scaling, fault segmentation, and structural maturity, *Earth Planet. Sci. Lett.*, *253*(3), 429–438.

Mann, P., F. Taylor, R. L. Edwards, and T.-L. Ku (1995), Actively evolving microplate formation by oblique collision and sideways motion along strike-slip faults: An example from the Northeastern Caribbean plate margin, *Tectonophysics*, *246*(1), 1–69.

Mann, P., E. Calais, J.-C. Ruegg, C. DeMets, P. E. Jansma, and G. S. Mattioli (2002), Oblique collision in the Northeastern Caribbean from GPS measurements and geological observations, *Tectonics*, *21*(6), 1057, doi:10.1029/2001TC001304.

Mavroeidis, G. P., and C. M. Scotti (2013), Finite-fault simulation of broadband strong ground motion from the 2010 Mw 7.0 Haiti earthquake, *Bull. Seismol. Soc. Am.*, *103*(5), 2557–2576.

McCann, W. R. (2006), *Estimating the Threat of Tsunamogenic Earthquakes and Earthquake Induced-Landslide Tsunami in the Caribbean*, World Sci., Singapore.

Meng, L., J.-P. Ampuero, A. Sladen, and H. Rendon (2012), High-resolution backprojection at regional distance: Application to the Haiti *M*7.0 earthquake and comparisons with finite source studies, *J. Geophys. Res.*, *117*, B04313, doi:10.1029/2011JB008702.

Mercier de Lépinay, B., et al. (2011), The 2010 Haiti earthquake: A complex fault pattern constrained by seismologic and tectonic observations, *Geophys. Res. Lett.*, *38*, L22305, doi:10.1029/2011GL049799.

Nettles, M., and V. Hjörleifsdóttir (2010), Earthquake source parameters for the 2010 January Haiti main shock and aftershock sequence, *Geophys. J. Int.*, *183*(1), 375–380.

Oglesby, D. D. (2005), The dynamics of strike-slip step-overs with linking dip-slip faults, *Bull. Seismol. Soc. Am.*, *95*(5), 1604–1622.

Oglesby, D. D., S. M. Day, Y.-G. Li, and J. E. Vidale (2003), The 1999 Hector Mine earthquake: The dynamics of a branched fault system, *Bull. Seismol. Soc. Am.*, *93*(6), 2459–2476.

Olson, S. M., R. A. Green, S. Lasley, N. Martin, B. R. Cox, E. Rathje, J. Bachhuber, and J. French (2011), Documenting liquefaction and lateral spreading triggered by the 12 January 2010 Haiti earthquake, *Earthquake Spectra*, *27*(S1), S93–S116.

Oppenheimer, D. H. (1990), Aftershock slip behavior of the 1989 Loma Prieta, California earthquake, *Geophys. Res. Lett.*, *17*(8), 1199–1202.

Prentice, C., P. Mann, A. Crone, R. Gold, K. Hudnut, R. Briggs, R. Koehler, and P. Jean (2010), Seismic hazard of the Enriquillo-Plantain Garden fault in Haiti inferred from palaeoseismology, *Nat. Geosci.*, *3*(11), 789–793.

Ratchkovski, N. A., S. Wiemer, and R. A. Hansen (2004), Seismotectonics of the central Denali fault, Alaska, and the 2002 Denali fault earthquake sequence, *Bull. Seismol. Soc. Am.*, *94*(6B), S156–S174.

Symithe, S. J., E. Calais, J. S. Haase, A. M. Freed, and R. Douilly (2013), Coseismic slip distribution of the 2010 M 7.0 Haiti earthquake and resulting stress changes on regional faults, *Bull. Seismol. Soc. Am.*, *103*(4), 2326–2343.

Wessel, P., and W. H. Smith (1998), New, improved version of generic mapping tools released, *Eos Trans. AGU*, *79*(47), 579–579.